

## Fast waveform inversion strategies applied to Hussar

Marcelo Guarido\*, Raul Cova\*, Sergio J. Romahn\*, Laurence R. Lines\*, Robert J. Ferguson†, Kristopher A. H. Innanen\*

### ABSTRACT

The Fast Waveform Inversion (FastWI) is a linear solution of the Full Waveform Inversion. It is fast, as it is applied on post-stack data, and does not require any forward modeling. The gradient is calibrated by available sonic logs. We tested the inversion to apply an acoustic inversion on the vertical component of the processed Hussar data. The inversion is driven and compared with three sonic logs acquired over the 2D line. The inverted P-wave velocities show consistency in the well location and with the stacked section, with the clear limitations of the acoustic inversion on elastic data. Also, we noticed that the calibration is only effective in areas with high signal-to-noise ratio in the stacked section.

### INTRODUCTION

Seismic inversion techniques are the ones that use intrinsic informations contained in the data to determine rock properties by matching a model that "explains" the data. Some examples are the variation of amplitude per offset, or AVO (Shuey, 1985; Fatti et al., 1994), the traveltime differences between traces, named traveltime tomography (Langan et al., 1984; Bishop and Spongberg, 1984; Cutler et al., 1984), or even by matching synthetic data to the observed data, as it is done in full waveform inversion (Tarantola, 1984; Virieux and Operto, 2009; Margrave et al., 2010; Pratt et al., 1998), among others. These inversions can compute rock parameters as P and S waves velocities, density, viscosity and others. In this work we are focused in the inversion of the P wave velocity.

FWI is a least-square based inversion, which objective is to find the model parameters that minimizes the difference between observed (acquired) and synthetic shots (Margrave et al., 2011), or the residuals. This is accomplished in an iterative fit method by linearizing a non-linear problem. It is an algorithm similar to a *Ridge Regression* (Chipman, 1999), which minimizes non-linear problems by adding a regularization term to avoid over fitting (to smooth the model). In seismic processing, I regularize the inversion by convolving the model with a 2D Gaussian window (Margrave et al., 2010).

The full waveform inversion was proposed in the early 80's (Pratt et al., 1998) but the technique was considered too expensive in computational terms. Lailly (1983) and Tarantola (1984) simplified the methodology by using the steepest-descent method (or gradient method) in the time domain to minimize the objective function without calculate, explicitly, the partial derivatives. They compute the gradient by a reverse-time migration (RTM) of the residuals. Pratt et al. (1998) develop a matrix formulation for the full waveform inversion in the frequency domain and present more efficient ways to compute the gradient and the inverse of the Hessian matrix (the sensitive matrix) the Gauss-Newton or the Newton

---

\*CREWES - University of Calgary

†University of Calgary

approximations. The FWI is shown to be more efficient if applied in a multi-scale method, where lower frequencies are inverted first and is increased as more iterations are done (Pratt et al., 1998; Virieux and Operto, 2009; Margrave et al., 2010). An overview of the FWI theory and studies are compiled by Virieux and Operto (2009). Lindseth (1979) showed that an impedance inversion from seismic data is not effective due to the lack of low frequencies during the acquisition but could be compensated by the match with a sonic-log profile. Warner and Guasch (2014) use the deviation of the Weiner filters of the real and estimated data as the object function with great results. Margrave et al. (2010) and Romahn and Innanen (2016) calibrate the gradient by matching it with sonic logs, estimating a more precise step length and avoiding cycle skipping. They also use the Gazdag and Sguazzero (1984) PSPI migration algorithm with a deconvolution imaging condition (Margrave et al., 2011; Wenyong et al., 2013) to migrate the residuals faster than the RTM, but preserving the gradient's resolution. Guarido et al. (2015) use the PSPI migration to migrate each frequency content of the residuals independently, generating a pseudo-gradient for each frequency and then averaging stacking them, using the step length as weight. It resulted on a highly detailed model, but the computation costs are high. Guarido et al. (2016) apply an impedance inversion in the gradient to improve the resolution of the inverted model. Guarido et al. (2016, 2017b) propose a simpler approximation for the gradient that does not require any forward modeling, by linearizing the problem. They just apply a PSPI migration on the acquired data and compare the result with the current model. The methodology was also extended for a post-stack depth migration, the *Fast Waveform Inversion*, or FastWI. However, two forward modeling are required to estimate the step length. Guarido et al. (2017a) proposes to combine the forward modeling-free gradient method with the well calibration of Margrave et al. (2010) and Romahn and Innanen (2016) to obtain a fast waveform inversion that doesn't require any forward modeling and source estimation, it only requires the PSPI migration of the acquired data (that can be pre or post stack). Guarido et al. (2017c) compare the use of the RTM and PSPI migrations in the estimation of the gradient for the FastWI, showing that the choice depends on how complex is the velocity model and the computational power available.

Many efforts were done in the past to retrieve the impedance inversion from the Hussar low frequency seismic data. Gavotti et al. (2012) applies a model-based inversion, which estimates the impedance that minimize the the difference between current impedance to the sonic-log, and focused the interpretation at the target zone (around 1.2s). Lloyd and Margrave (2012) applies a band-limited impedance inversion using the stacking velocity to fill the low frequency gap of the seismic data, providing a very consistent model. Saeed et al. (2014) analyze the acoustic and elastic properties of the inversion by applying pre-stack (AVO) and post-stack inversions. Wenyong et al. (2015) shows that the application of the FWI in the Hussar data improves the reverse-time migrated image.

In this report, we are applying the FastWI in the Hussar data to obtain the acoustic (P-wave) model of the subsurface. We show how the vertical components of the data are processed to obtain the stacked section to be the input data of the inversion. Three sonic logs are used to create the initial model (an interpolation of their linear trend), and to guide the direction and calibration of the gradient. As the stacked section shows to be composed mostly by horizontally flat reflectors, we use a zero-offset PSPI migration to estimate the gradient, as it is cheaper but preserves the resolution when compared to the RTM (Guarido

et al., 2017c).

## THEORY

### The steepest-descent method

The FastWI has its origins in the FWI, by linearizing the seismic processes involved to obtain the gradient in the steepest-descent method. The objective function of the FWI method is (Tarantola, 1984):

$$C(\mathbf{m}) = \|\mathbf{d}_0 - \mathbf{d}(\mathbf{m})\|^2 = \|\Delta\mathbf{d}(\mathbf{m})\|^2 \quad (1)$$

where  $\Delta d$  is the data residual (the difference between acquired and synthetic shots),  $m$  is the model (in this work, the P-wave velocity) and  $\|\cdot\|$  represents the norm-2 of the array. The minimization is done by calculating the Taylor's expansion of the objective function of the equation 1 around a perturbation  $\delta m$  of the model and taking the derivative equal to zero (Tarantola, 1984; Pratt et al., 1998; Virieux and Operto, 2009). The solution is:

$$\mathbf{m}_{n+1} = \mathbf{m}_n - H_n^{-1} \mathbf{g}_n \quad (2)$$

where  $H$  is the Hessian (or sensitive matrix),  $g$  is the gradient computed by back-propagating the data residual and  $n$  is the  $n$ -th iteration. It is known as the Newton method. For the steepest-descent method, the Hessian matrix can be neglected and be equalized to the identity matrix:

$$\mathbf{m}_{n+1} = \mathbf{m}_n - \alpha_n \mathbf{g}_n \quad (3)$$

where  $\alpha$  is the step length, which can be determined by a line search or a least squares minimization (Pica et al., 1990). At this part, the gradient is understood as the reverse-time migration of the residuals. We can interpret this step and expand its meaning to say that the gradient is equivalent to a pre-stack depth migration of the residuals, and we decided to use a PSPI migration of the residuals with a deconvolution imaging condition (Margrave et al., 2010, 2011; Wenyon et al., 2013; Guarido et al., 2014).

### The forward modeling-free gradient

Computing the gradient requires three very known seismic processing steps: PSDM of the residuals, stacking and impedance inversion. Let's understand those steps as the operators  $M$  for migration,  $S$  for stacking and  $I$  for impedance inversion. Equation 3 can be re-written as:

$$\begin{aligned}
 \mathbf{m}_{n+1} &= \mathbf{m}_n - \alpha_n \mathbf{g}_n \\
 &= \mathbf{m}_n - \alpha_n I \{S [M (\Delta \mathbf{d}(\mathbf{m}_n))]\} \\
 &= \mathbf{m}_n - \alpha_n I \{S [M (\mathbf{d}_0 - \mathbf{d}(\mathbf{m}_n))]\}
 \end{aligned} \tag{4}$$

where  $\Delta \mathbf{d}(\mathbf{m}_n)$  is the n-th iteration residual  $\mathbf{d}_0 - \mathbf{d}(\mathbf{m}_n)$ ,  $\mathbf{d}_0$  is the acquired data,  $\mathbf{d}(\mathbf{m}_n)$  is the synthetic data of the n-th iteration and  $\mathbf{m}_n$  is the n-th iteration inverted model. For simplification and easier visualization, let's set  $\mathbf{d}(\mathbf{m}_n) = \mathbf{d}_n$ . Then equation 4 is:

$$\mathbf{m}_{n+1} = \mathbf{m}_n - \alpha_n I \{S [M (\mathbf{d}_0 - \mathbf{d}_n)]\} \tag{5}$$

Considering the linearity property of the migration operator (see appendix), the acquired and synthetic shots can be migrated separately:

$$\mathbf{m}_{n+1} = \mathbf{m}_n - \alpha_n I \{S [M (\mathbf{d}_0) - M (\mathbf{d}_n)]\} \tag{6}$$

The next step is to use the linearity property of the stacking operator and equation 6 becomes:

$$\mathbf{m}_{n+1} = \mathbf{m}_n - \alpha_n I \{S [M (\mathbf{d}_0)] - S [M (\mathbf{d}_n)]\} \tag{7}$$

The impedance inversion operator is *approximately* linear if we assume that the Earth's impedance follow a linear trend (small reflection coefficients) and a Taylor expansion of the reflection coefficients is used to estimate the update as a perturbation of Earth's impedance, ending up with another solution for equation 7:

$$\mathbf{m}_{n+1} = \mathbf{m}_n - \alpha_n (I \{S [M (\mathbf{d}_0)]\} - \underbrace{I \{S [M (\mathbf{d}_n)]\}}_{\text{Current model}}) \tag{8}$$

Again, on the second hand of the gradient approximation we have the model of the current iteration  $\mathbf{m}_n$ . Then equation 8 is simplified to:

$$\mathbf{m}_{n+1} = \mathbf{m}_n - \alpha_n (I \{S [M (\mathbf{d}_0)]\} - \mathbf{m}_n) \tag{9}$$

Equation 9 understand the gradient as a residual impedance inversion of the acquired data relative to the current model. The objective function is being minimized on the estimation of the step length, that requires 2 forward modeling when using Pica et al. (1990)'s approximation.

Looking again at equation 9, we understand that we are estimating the gradient by applying a sequence seismic processing tools. If we think about migration and stack, migrating the data and stacking should have the same effect as doing the inverted process (the pre and post stack migrations outputs have the same physical meaning: an image of the reflection coefficients of the subsurface). Then equation 9 is equivalent to:

$$\mathbf{m}_{n+1} = \mathbf{m}_n - \alpha_n (I \{M [S (\mathbf{d}_0)]\} - \mathbf{m}_n) \quad (10)$$

This means we can input in the algorithm a stacked section (figure 1) and apply a post-stack depth migration algorithm (we used a zero-offset based PSPI with a cross-correlation imaging condition). The stacking velocity is obtained by a velocity analysis. The direct arrivals are removed (muted) to avoid artifacts in the shallow area, but it means that the inversion is not effective in the near surface (as some primaries ended up muted as well).

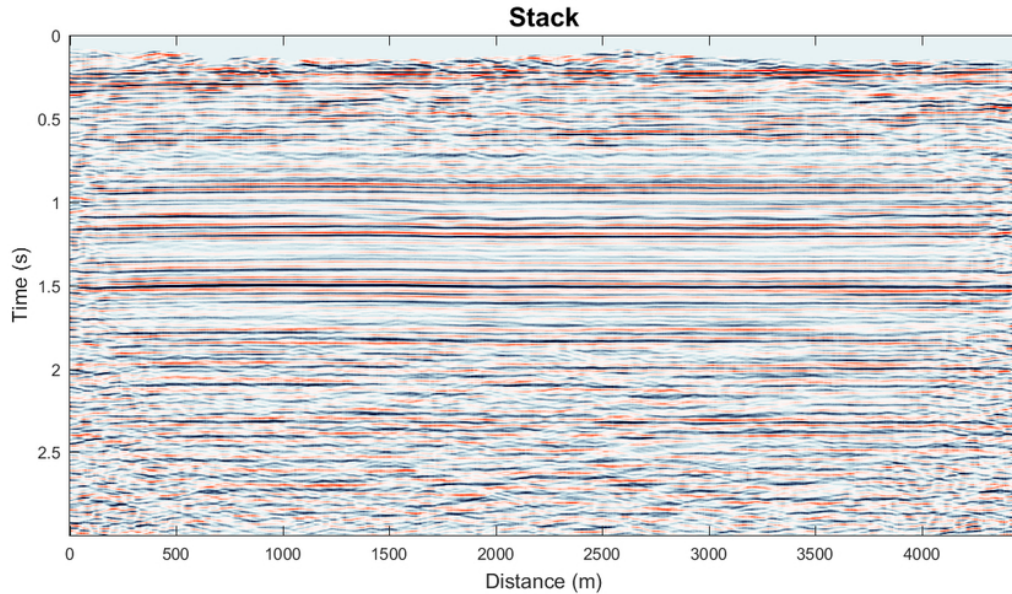


FIG. 1. Hussar stacked section used as input in the FastWI. The geology looks to be formed by horizontally flat layers.

Analyzing the Hussar stacked section on figure 1, we can observe the presence of noise in the shallow and deeper portions and also in the borders (where the fold is not maximum). Also, the reflectors are mostly horizontally flat and continuous (thanks to the application of a static correction).

## Well calibration

Until now we are assuming Pica et al. (1990)'s approximation to determine the step length on equations 9 and 10. However, it goes against our seeking for a forward modeling-free routine, as they still require two forward modeling to estimate the step length. Margrave et al. (2010) and Romahn and Innanen (2016) calibrate the gradient by matching it with a sonic log at the same spatial location. They estimate a scalar and phase rotation to

create a match filter to convolve with the gradient. This would lead us with a FWI algorithm 100% forward modeling-free. So we decided to implement it.

To find the scalar  $\alpha$  that minimizes the impedance inverted gradient trace  $S_{grad}$  to the impedance (sonic log) well trace  $S_{well}$ , we minimize the L2-norm function for  $\alpha$ :

$$\Phi = ||S_{well} - \alpha S_{grad}||^2 \quad (11)$$

This leads to a simple equation to estimate  $\alpha$ :

$$\alpha = \frac{S_{well}^T S_{grad}}{S_{grad}^T S_{grad}} \quad (12)$$

For the phase rotation, we use the *Toolbox* code *constphase.m* that finds the angle  $\phi$  that makes  $S_{grad}$  looks like  $S_{well}$ . By finding  $\alpha$  and  $\phi$ , we create a matching filter which is convolved with the gradient to have the model update.

Combining the well tie calibration with the forward modeling-free gradient of equations 9 and 10, we are proposing a new FWI routine that is 100% forward modeling-free. This reduces significantly the cost of the inversion without the need of the source estimation.

## FAST WAVEFORM INVERSION APPLIED TO THE HUSSAR SEISMIC DATA

### Hussar seismic survey

The FWI approach developed in this study was applied on the Hussar 2D-3C dataset. The survey was conducted near Hussar in Central Alberta at approximately 100 Km east of Calgary. These data consist of 257 source stations spaced every 20 m approximately and, 448 receiver stations spaced every 10 m, for total length of 4.47 Km. Although originally acquired with a variety of sources and receivers (Margrave et al., 2012), in this study we only use the vertical component of the accelerometer data recorded using 2 kg dynamite sources at 15 m depth. Figure 2 shows the source and receiver distribution in the area and the location of the wells used in this study.

All receivers were live at every source point producing source gathers with 448 traces. This configuration resulted in a fold profile that increases gradually up to a maximum value of 257 at the centre of the line.

### Preconditioning processing flow

The processing workflow applied on the Hussar data is summarized on Figure 3. The processing sequence featured what we consider a standard 2D processing workflow.

After the data were loaded and the survey geometry was setup, we proceeded to pick the first arrivals and compute a static solution. A weathering velocity of 800 m/s was fixed

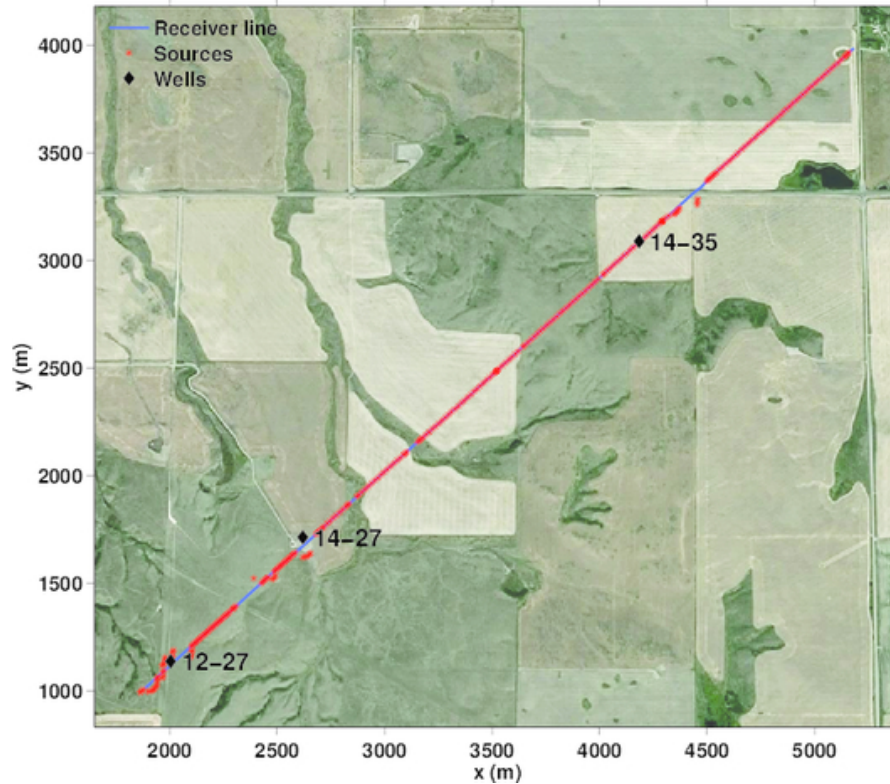


FIG. 2. Survey geometry and wells location.

and a replacement velocity of 3000 m/s was chosen according to the velocities observed on the first arrivals. Elevations were smoothed using a moving average with a length of 200 m to define a floating datum. Static corrections to the floating datum were later used for performing velocity analysis. The final datum was set slightly above the maximum elevation present in the data at 1000 above sea level.

Bad traces and spikes were then removed from the data. The surface-wave noise was filtered using a low pass filter in the radial trace domain (Henley, 1999) to isolate linear noise with apparent velocities of less than 1000 m/s. The noise data were then subtracted from the input data to remove the surface-wave train.

Using an initial NMO velocity analysis, a velocity function was defined and then used to compute an spherical divergence correction of the form  $1/[v(t)t]^2$ , where  $v(t)$  denotes the velocity function and  $t$  is the sample time. To compensate for additional amplitude distortions due to source and receiver conditions a surface-consistent amplitude balancing was performed.

On the same way, to remove the spectral signature of the sources and receivers, a surface-consistent spiking deconvolution with an operator length of 200 ms was performed. After redatuming the data to the floating datum a velocity analysis was performed. The CMP gathers were then NMO-corrected and a surface-consistent residual statics correction was computed.

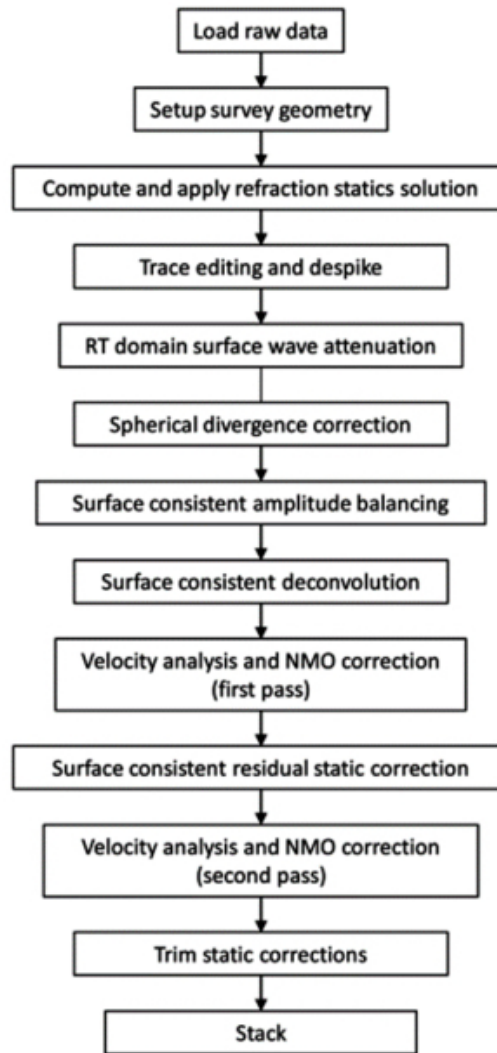


FIG. 3. Processing work-flow applied to the Hussar dataset.

After removing residual statics a new velocity function was picked and numerical or trim static corrections were applied in order to enhance the stacking power of the data. Finally, a stacked section was produced.

Since the FWI approach used in this study relies on the stacked data, further processing was applied to enhance the coherency of the events in the section and attenuate the presence of noise. The processing used in this part of the work-flow is outlined in Figure 4.

To compensate for the change in bandwidth with time, a time-variant spectral balancing was performed. Since no significant structural deformations were expected in these data an F-K filter designed to remove dipping events was applied. Then, an FX prediction filter was used to enhance the coherency of the events. In this case 25% of the data before applying the filter was added back to the output. An automatic gain control (AGC) correction, with a window of 500 ms was then applied to minimize amplitude distortions. Finally, a band pass filter between 3 Hz and 70 Hz was applied to generate the final stacked section.

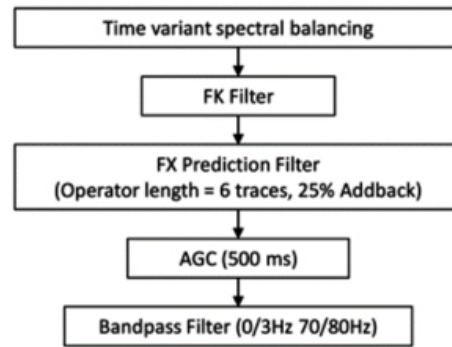


FIG. 4. Stacked section post-processing work-flow.

### Fast waveform inversion applied to 2D Hussar

For the FastWI, the input data is the Hussar stacked section of figure 1. The inversion consists on migration the stacked section using a zero-offset PSPI migration to obtain the "current model impedance" of equation 10. For that, we start the inversion using the velocity model of figure 5. This velocity is a 2D cubic interpolation of the linear trend of the sonic logs "12-27", "14-27" and "14-35" (figure 11), which spacial positions are shown on figure 5.

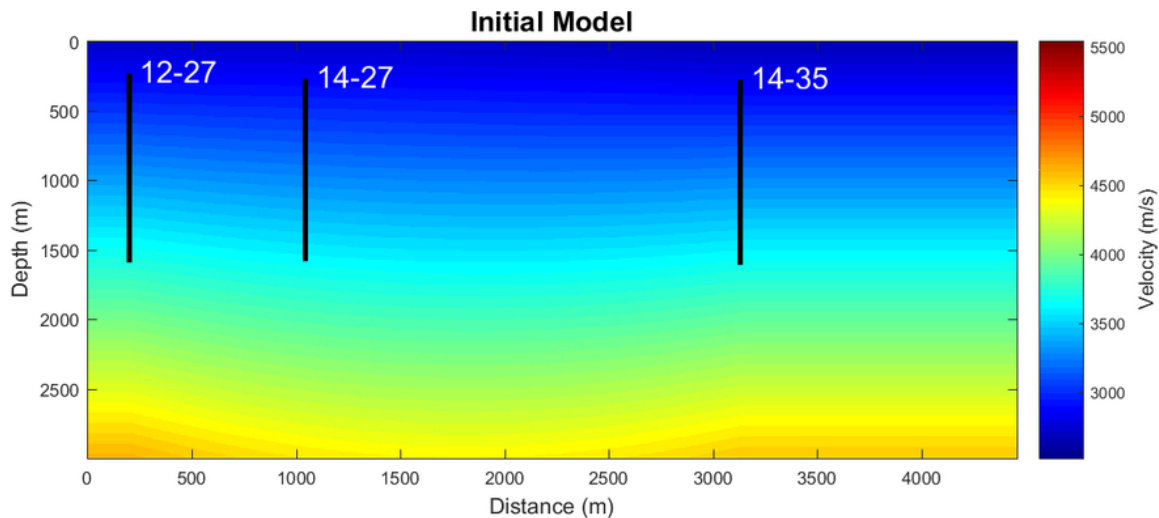


FIG. 5. The initial model used for the inversion. It is a 2D cubic interpolation of the linear trends of the sonic logs from wells "12-27", "14-27" and "14-35", also shown on figure 11.

We are applying a multi-scale inversion (start with lower frequencies and later invert higher frequencies). However, simply by experience (Guarido et al., 2014, 2015, 2016), we fell comfortable to invert frequency bands with amplitude above  $-20dB$ . We plotted the amplitude spectrum of the 2D Hussar stacked section on figure 6, and this frequency band is around  $8Hz$  to  $48Hz$ , but we decided to pick the band of  $4-48Hz$ . We observed that, for frequencies down to  $4Hz$ , impedance information can still be recovered, but this did not show to be the case for higher frequencies. For even lower frequencies ( $1-3Hz$ ), we believe it is already included in the initial model.

After deciding on which frequencies we will work, now we have to decide on *how* to

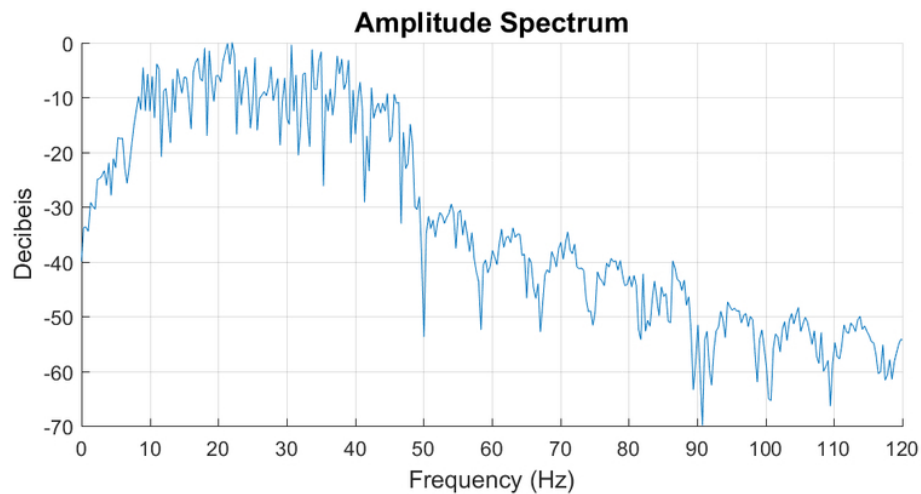


FIG. 6. Amplitude spectrum of the stacked section of figure 1. The FastWI is applied to the frequencies with amplitude above -20dB.

use them. Back to the multi-scale method, we migrate first a small frequency band of the stacked section, starting from  $4-6\text{Hz}$ , and, at each iteration, we add  $1\text{Hz}$  to this frequency vector. The gradient is then obtained as proposed on equation 10 at the specific current frequency band. The conjugate gradient is then computed (Guarido et al., 2015), just before preconditioning the gradient by convolving it with a 2D Gaussian window (Margrave et al., 2010; Guarido et al., 2014). The final step before updating the model is to calibrate the gradient using the sonic logs of figure 11. A matching filter is created at each well location and then they are interpolated, ending up with one matching filter per CDP. To obtain the model update, the matrix of matching filters is trace-by-trace convolved with the gradient.

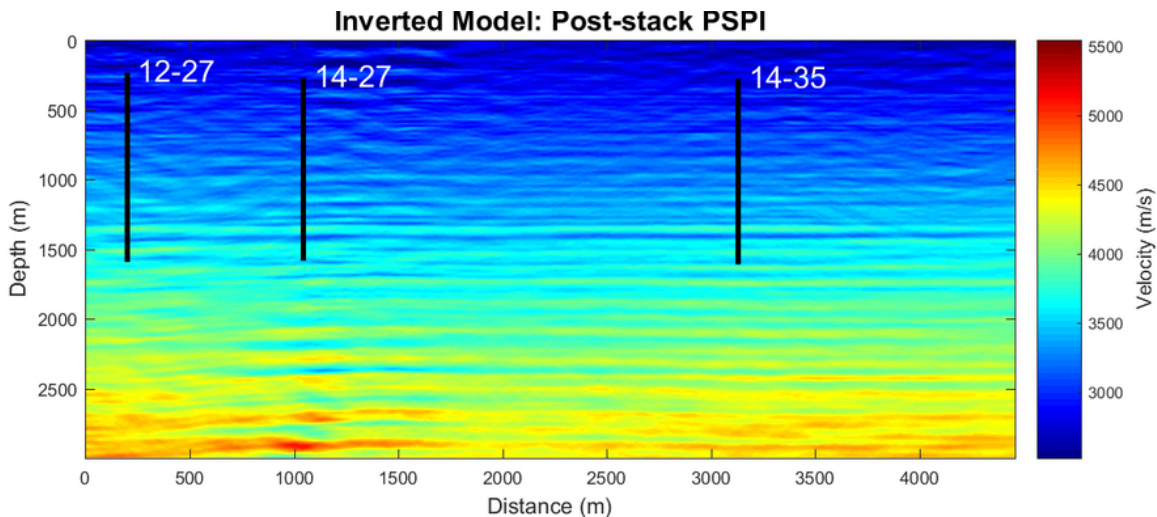


FIG. 7. Inverted model for the 2D Hussar stacked section. Vertical stripes are present in the deeper portion of the model, and at near-surface, where the seismic data is muted during the stacking process and another mute is applied on shots to eliminate the direct arrivals, the inversion is not effective and only some stretched events are observed. At shallow and middle depths, where the wells reach, the inversion looks consistent with the stacked section and wells.

Figure 7 shows the inverted model for the 2D Hussar stacked section. Vertical stripes are present in the deeper portion of the model, and at near-surface, where the seismic data

is muted during the stacking process and another mute is applied on shots to eliminate the direct arrivals, the inversion is not effective and only some stretched events are observed. At shallow and middle depths, where the wells reach, the inversion looks consistent with the stacked section and wells. Figures 8 and 9 show, respectively, a zoom of the initial and inverted models for the depth range of 0 to 1600m.

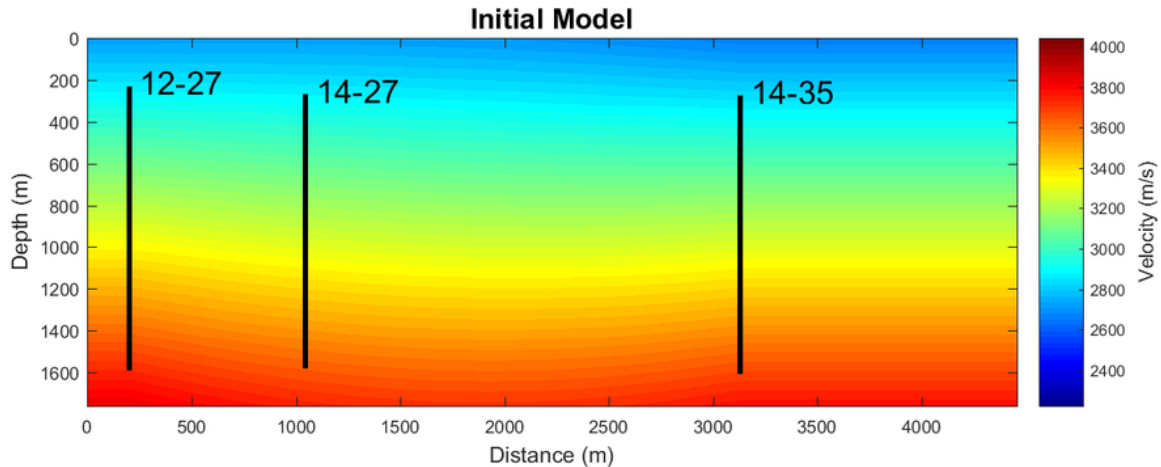


FIG. 8. Zoomed initial model.

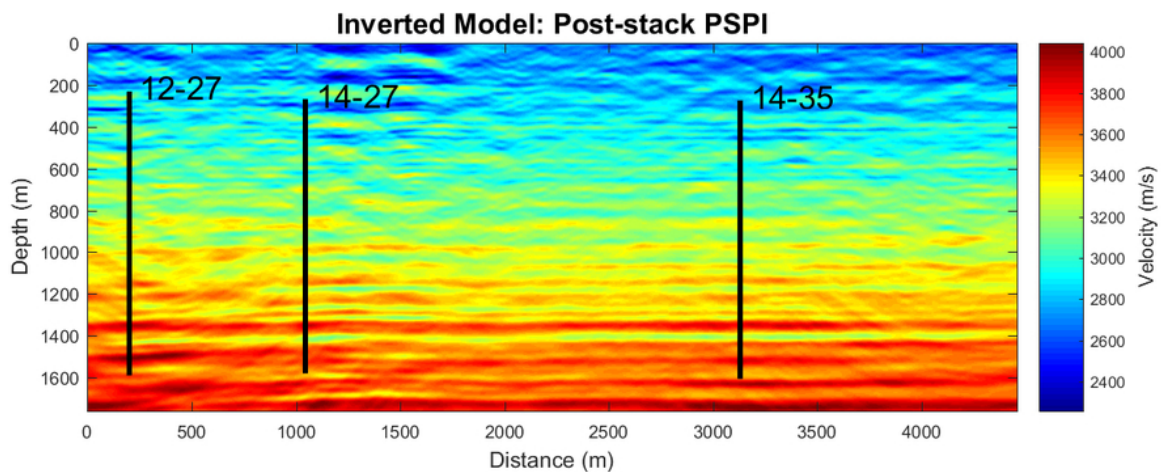


FIG. 9. Zoomed inverted model. Most of the recovered layers are horizontally flat.

On figure 9 the stretched events are more evident. In between the wells, most of the recovered layers are flat, and some hyperbolic artifacts are observed, probably resulted from the migration of refracted waves. We used the inverted model to migrate the full stacked section and plotted the result over the inverted model on figure 10. For the migration, due the stretch events at near surface, we replaced the first 300m of the inverted model by the starting velocity of figures 5 and 8.

The inverted model and migrated stack are composed of flat layers that follow the same trend. The consistency of the inverted velocities can be interpreted by comparing the inverted model with the sonic log. On figure 11 show the sonic log (black line), initial model (blue line) and inverted model (red line) at the wells "12-27", "14-27" and "14-35". Starting from the linear trend of the sonic logs, the FastWI was able to deliver an inverted model that

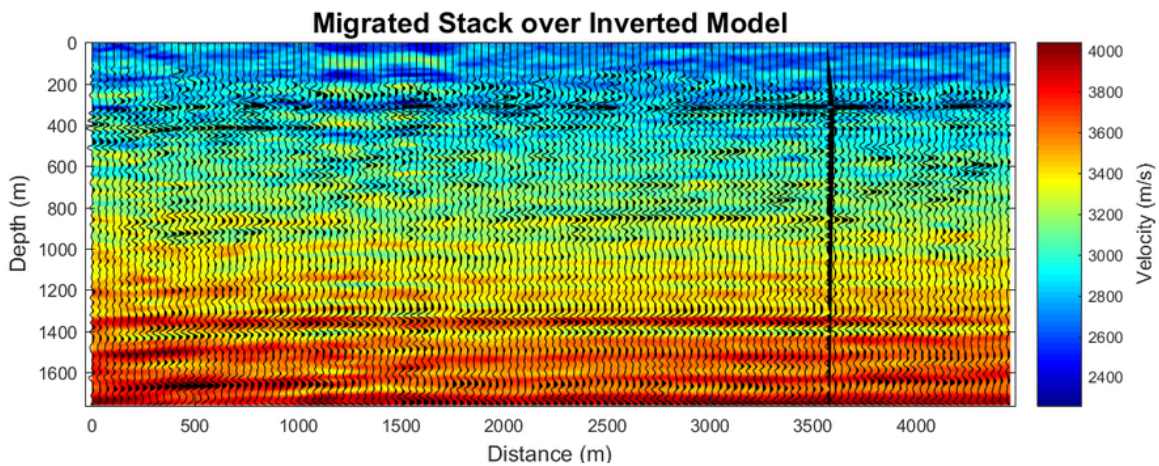


FIG. 10. Migrated stack over the inverted model. All the recovered data look to have correlation with the reflectors in the migrated data.

has a shape close to the sonic logs, matching in some areas, and missing some "amplitude" in others.

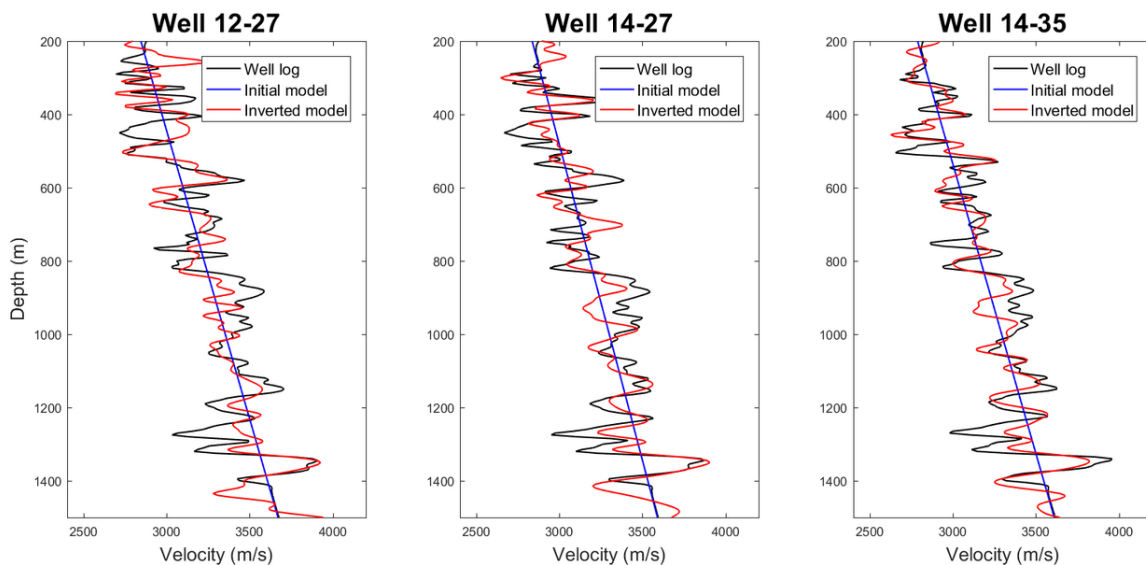


FIG. 11. Sonic log (black line), initial model (blue line) and inverted model (red line) at the wells "12-27", "14-27" and "14-35". Starting from the linear trend of the sonic logs, the FastWI was able to deliver an inverted model that has a shape close to the sonic logs, matching well in some areas, and missing some "amplitude" in others.

Figure 12 shows the deviation (normalized L2-norm) of the inverted model relative to the wells "12-27" (blue line), "14-27" (red line), "14-35" (black line) and the averaged deviation (magenta line). The deviation started from 1 at the initial model (the linear trend of the wells) and started to decrease at each iteration. The minimum average point of 0.62 is reached at the very last iteration (orange asterisk).

At this point, we used all the three wells in the match, and it looks obvious that the inverted model will give a low deviation at those locations. Now we will apply the FastWI using each of the well as "blind" (not used to match, only to compute the deviation). First,

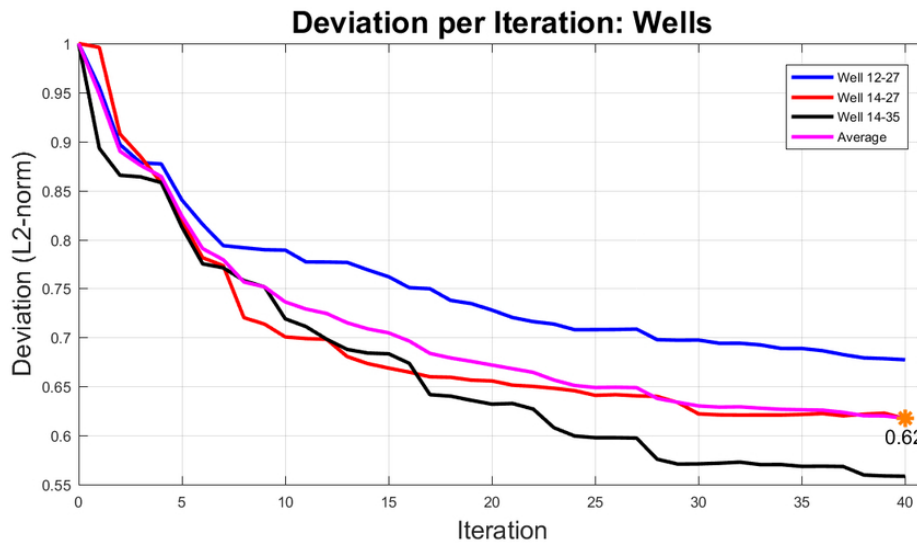


FIG. 12. Deviation (normalized L2-norm) of the inverted model relative to the wells "12-27" (blue line), "14-27" (red line), "14-35" (black line) and the averaged deviation (magenta line). The deviation started from 1 at the initial model (the linear trend of the wells) and started to decrease at each iteration. The minimum average point of 0.62 is reached at the very last iteration (orange asterisk).

the well "14-35" is left as the blind one. Figure 13 shows the zoomed inversion.

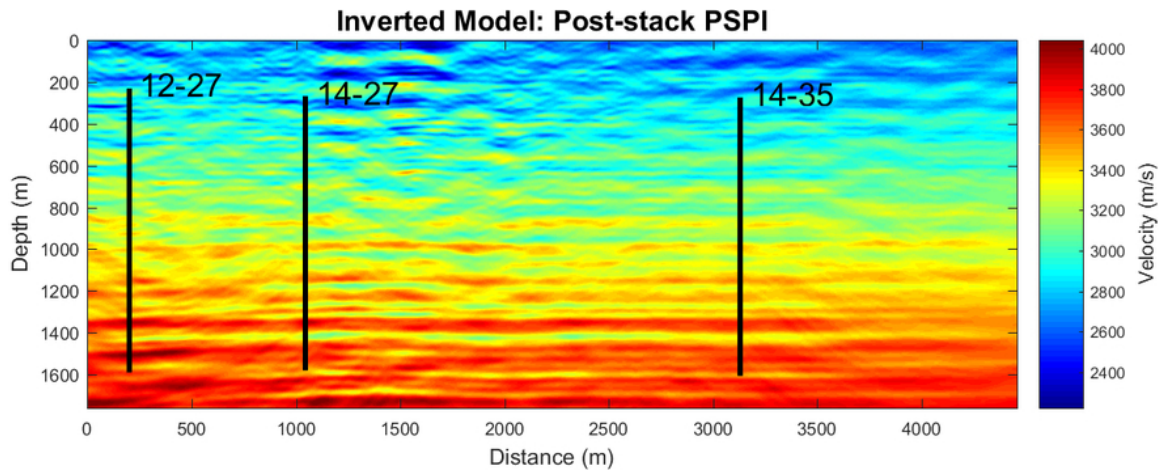


FIG. 13. Inverted model using well "14-35" as blind.

Not using the well "14-35" to calibrate the gradient gave a similar inversion as using the three wells. But we want to make sure that the matching filters obtained from wells "12-27" and "14-27" lead to a good inversion at the blind well location, and on figure 14 we show the deviation at the matching wells locations and at the blind well position.

By the way the interpolation of the matching filter is applied, the inversion at the blind well location ("14-35") is controlled by the matching at the well "14-27". It is interesting to check that the deviation decreases until the 8<sup>th</sup> iteration and becomes stable after that. It is possible to say that the matching filter selection at well "14-27" also works for, at least, the traces until well "14-35". On figure 15 compares the sonic log (black line) with the initial (blue line) and inverted (red line) models at the wells locations.

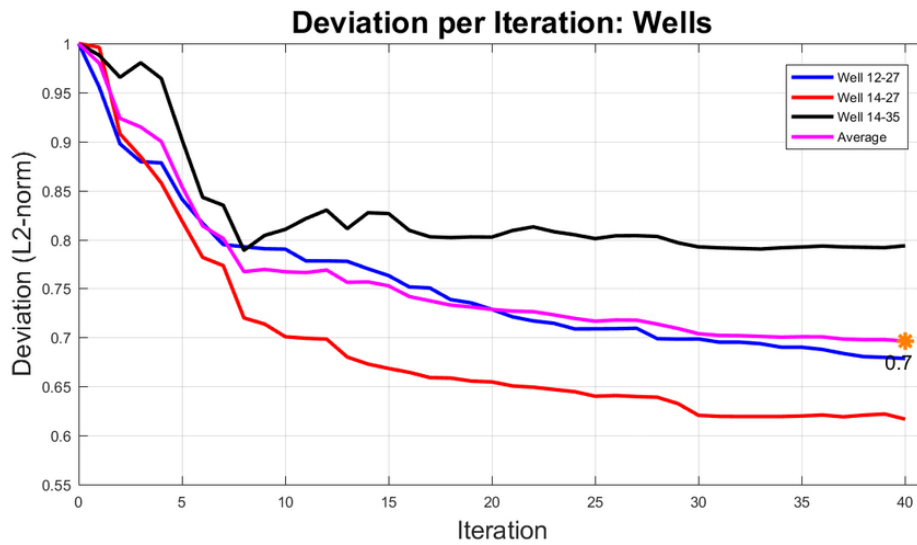


FIG. 14. Deviation (normalized L2-norm) of the inverted model relative to the wells "12-27" (blue line), "14-27" (red line), "14-35" (black line) and the averaged deviation (magenta line). The deviation started from 1 at the initial model (the linear trend of the wells) and started to decrease at each iteration. The deviation at the blind well ("14-35") shows to converge. The minimum average point of 0.7 is reached at the very last iteration (orange asterisk).

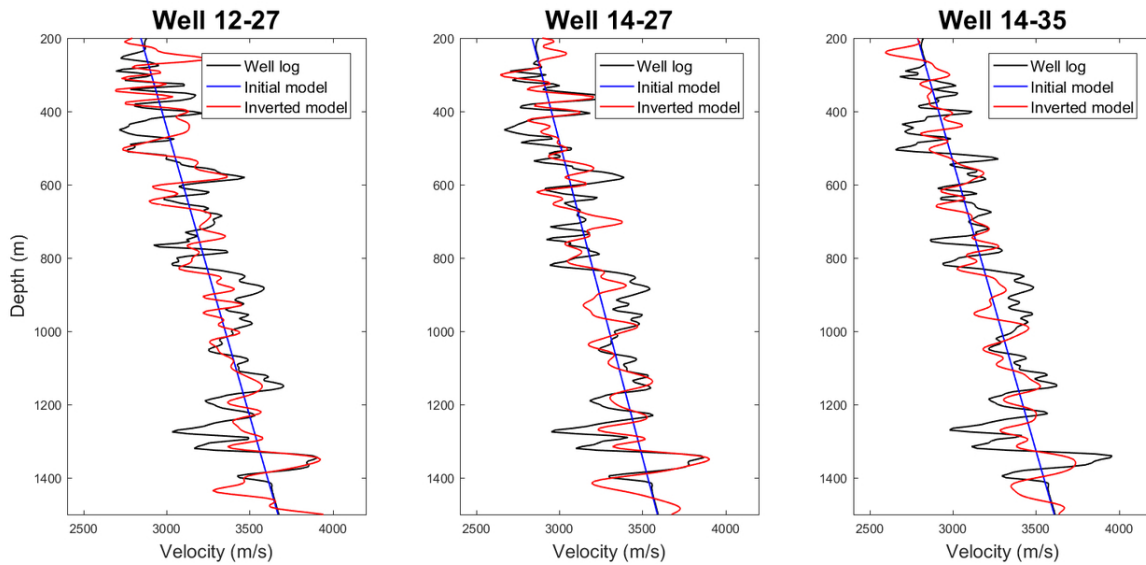


FIG. 15. Sonic log (black line), initial model (blue line) and inverted model (red line) at the wells "12-27", "14-27" and "14-35". The well "14-35" is used as blind, but the inverted model is in the direction to match the sonic log.

Even with no matching done at the blind well location, the inverted model tends to follow the trends of the sonic log (well "14-35"). Now, let's choose the well in the middle ("14-27") as the blind one. On figure 16 is plotted the inverted model without the calibration at the blind well location.

Once again, is really hard to evaluate the inversion precision by just looking to the model, but it has some differences close to the blind well location. The plot of the deviations at the wells locations is on figure 17.

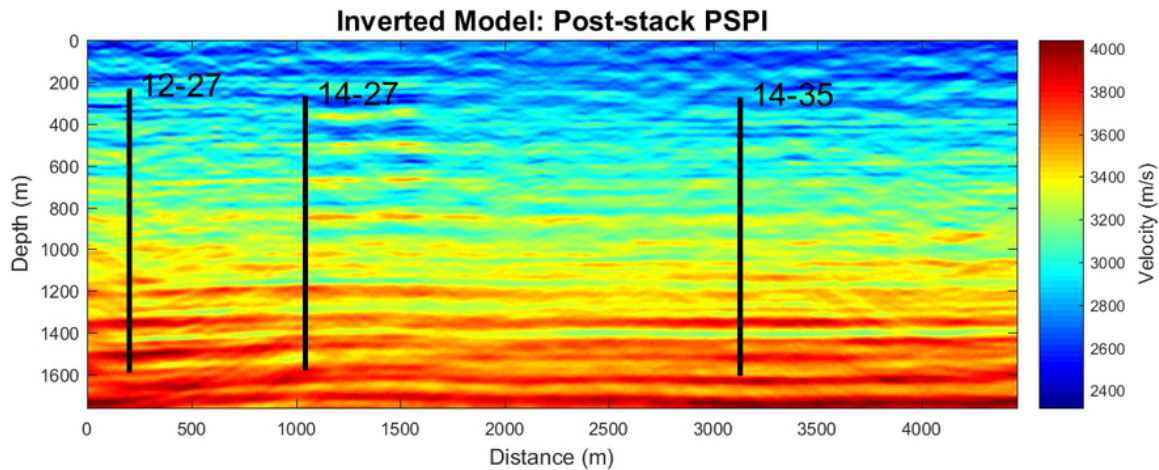


FIG. 16. Inverted model using well "14-27" as blind.

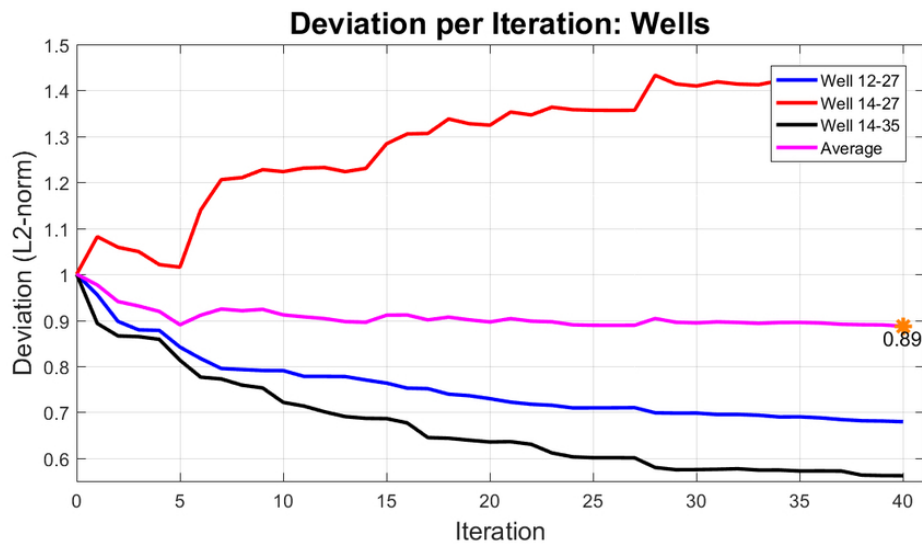


FIG. 17. Deviation (normalized L2-norm) of the inverted model relative to the wells "12-27" (blue line), "14-27" (red line), "14-35" (black line) and the averaged deviation (magenta line). The deviation at the blind well ("14-27") shows to diverge. The minimum average point of 0.89 is reached at the very last iteration (orange asterisk).

The inversion at the blind well location is dominated by the matching filter obtained at the closest well, that is, in this case, the "12-27", which is located at approximately 200m. Looking at the same spot in the stacked section (figure 1) the well "12-27" is located at a noisier region. This leads us to believe that, at this well, the method is trying to match noise, obtaining a poor matching filter. Apparently, we need to take this in consideration when applying the FastWI: we need to use wells that are close to areas in the stacked section that have high signal-to-noise ratio. On figure 18 are plotted the sonic logs comparison.

It is clear that the inversion failed at the blind well location. To validate the hypothesis of the matching noise at the well location, we are matching only the well "14-35", leaving the wells "12-27" and "14-27" as blind. The inverted model is shown on figure 19.

This new inverted model looks smoother than the others. And all the layers are flat.

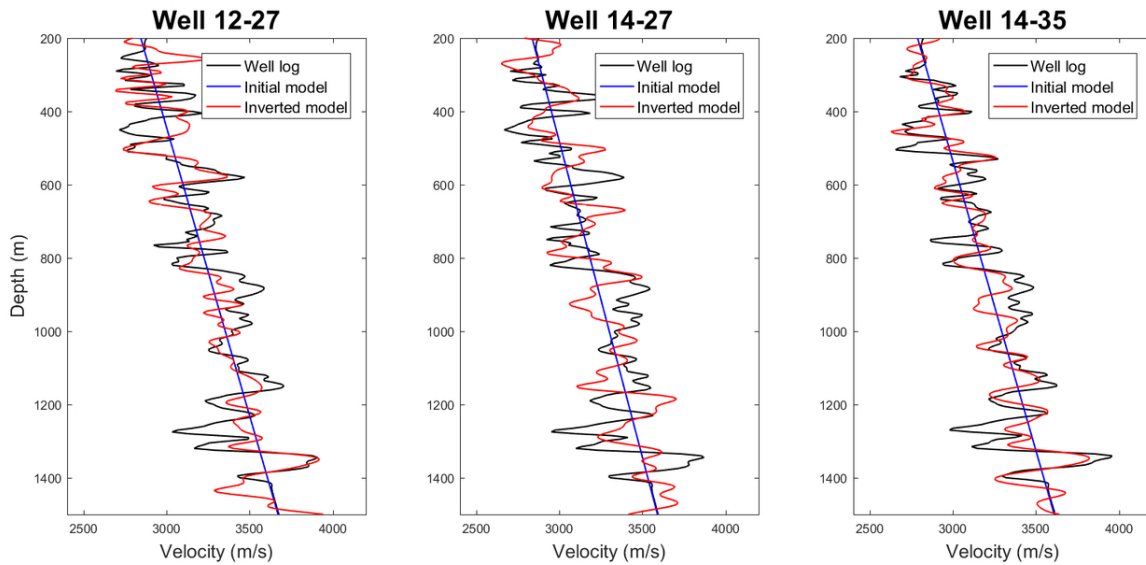


FIG. 18. Sonic log (black line), initial model (blue line) and inverted model (red line) at the wells "12-27", "14-27" and "14-35". The well "14-27" is used as blind, and the inversion at this point, dominated by the well "12-27", does not look to be effective.

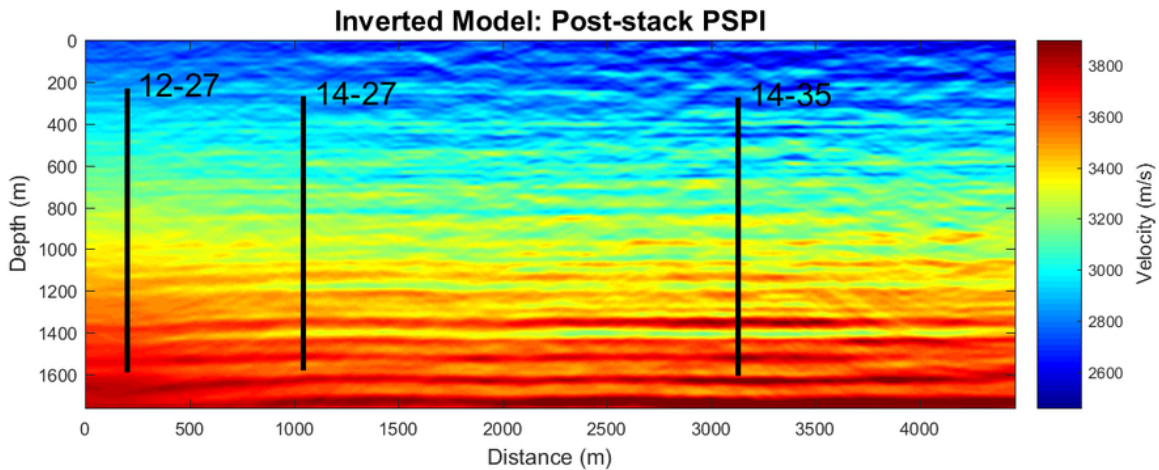


FIG. 19. Inverted model by matching the well "14-35" only.

Remembering that as only one well is used to calibrate the gradient, the inversion is driven by the matching filter obtained at this location. The deviation at the wells locations are plotted on figure 20.

The matching filter obtained at well "14-35" looks to work fine at the well "14-27", but not at well "12-27", which is the noisiest part of the stacked section. This looks to validate our hypothesis that noise is being matched at well "12-27" location. The comparison between sonic logs and initial and inverted models is shown on figure 21.

The inverted model at the well "14-35" seems to be a good match in the well "14-27" location, but the inversion also looks to be true (figure 15). The divergence in the deviation of the well "14-27" on figure 17 is due to the inversion at this area be dominated by the matching filter obtained at the well "12-27", while convergence is reached when

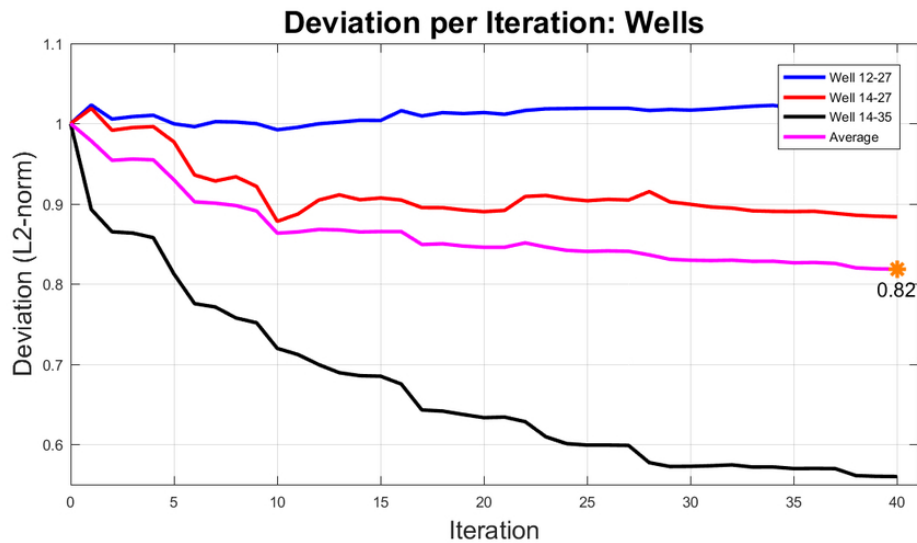


FIG. 20. Deviation (normalized L2-norm) of the inverted model relative to the wells "12-27" (blue line), "14-27" (red line), "14-35" (black line) and the averaged deviation (magenta line). The deviation at well "14-27" shows to converge, while it diverges at the well "12-27" location. The minimum average point of 0.82 is reached at the very last iteration (orange asterisk).

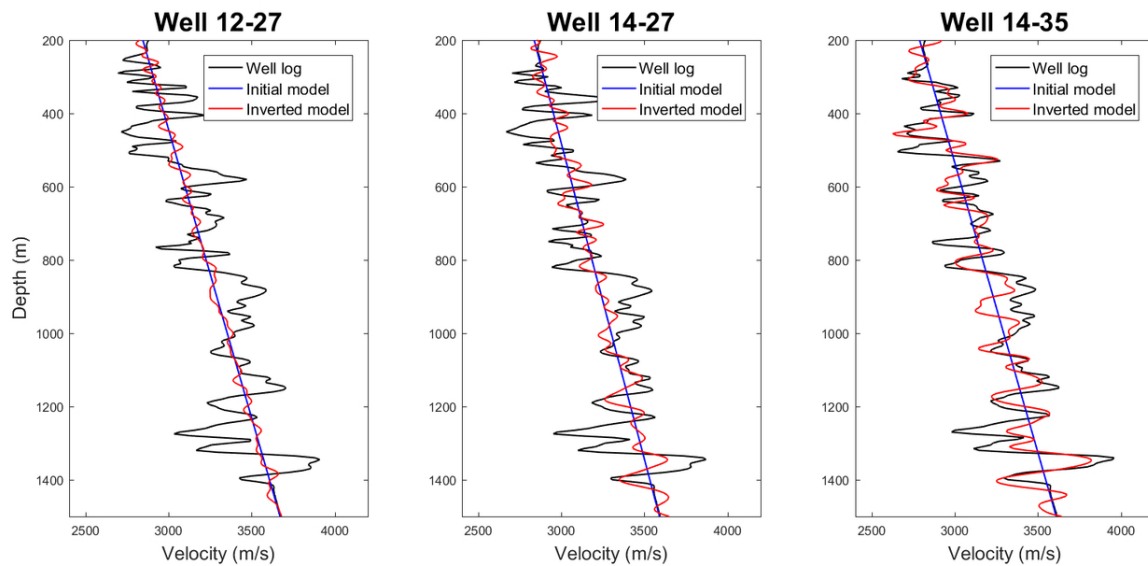


FIG. 21. Sonic log (black line), initial model (blue line) and inverted model (red line) at the wells "12-27", "14-27" and "14-35". The well "14-27" is used as blind, and the inversion at this point, dominated by the well "12-27", does not look to be effective.

the inversion is dominated by the matching filter obtained at the well "14-35". Assuming that the hypothesis of the noise match at well "12-27" is valid, and with the analysis that the matching filters from wells "14-27" and "14-35" work in areas away from the wells locations, we believe that the most reliable model is the one matching only the best two wells (figure 22).

The inverted model is obtained by the equivalent to use the well "12-27" as blind. We believe that the matching filter obtained at the wells "14-27" and "14-35" are stable to be used from the wells until the borders, and a linear interpolation is a reliable choice in

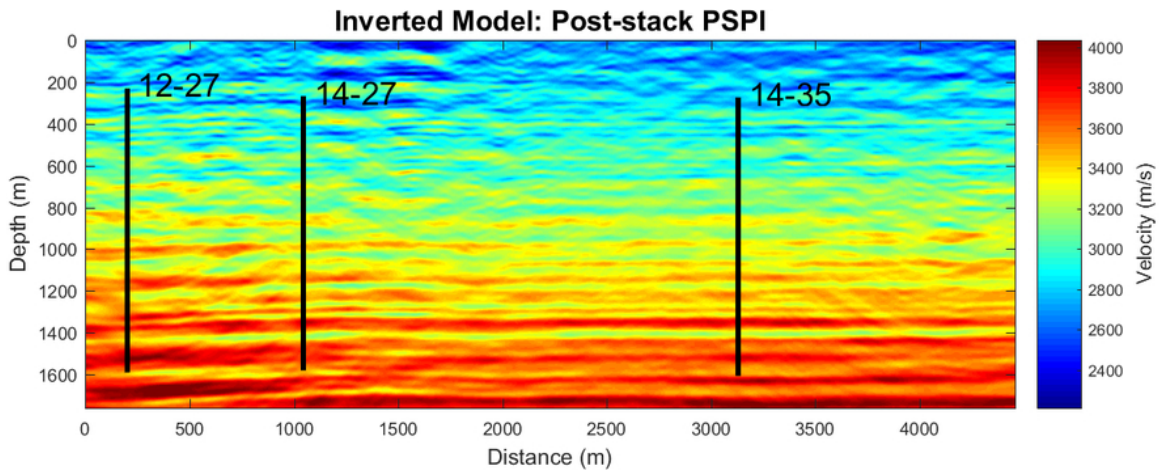


FIG. 22. Inverted model by matching the wells "14-27" and "14-35".

between the wells.

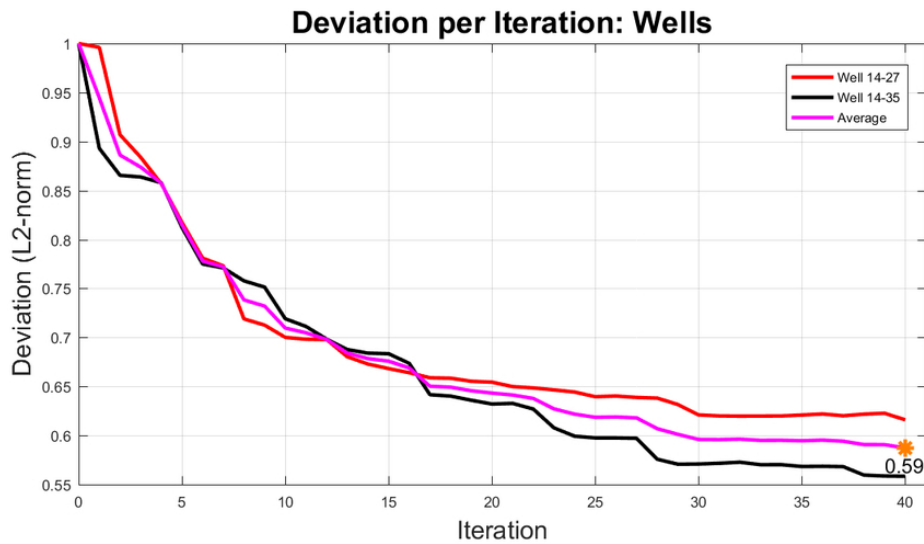


FIG. 23. Deviation (normalized L2-norm) of the inverted model relative to the wells "14-27" (red line), "14-35" (black line) and the averaged deviation (magenta line). The deviation converge at both wells (as they are used for the calibration). The minimum average point of 0.59 is reached at the very last iteration (orange asterisk).

Figure 23 is the deviation at the wells "14-27" and "14-35". They are the same as on figure 9. And the sonic log matching is also the same as the first test (figure 11) for the two wells used to calibrate the gradient.

Even with the limitations for the near-surface and that the method is an acoustic inversion applied on acquired data, it showed to converge to a reasonable P-velocity model that, by solving the lack of near-surface information, can be used to improve the seismic image. It also showed to run quickly, as the most costly seismic tool used is a post-stack migrations, and it may be a great solutions for 3D surveys as well.

## CONCLUSIONS

The *Fast Waveform Inversion* (FastWI) is a linear solution of the full waveform inversion, leading to a forward modeling-free method, and it can be performed with post-stack migration. The optimization is driven by calibrating the gradient with sonic logs.

The inverted model is consistent with the sonic logs and the stacked section, showing good resolution, considering it is an acoustic inversion applied to field data. The method showed to be stable, as the deviation (L2-norm) at the wells locations shows to converge. However, for now, the method is sensitive to direct arrivals, whose needed to be muted, and the lack of information at near-surface (due to the stretch mute), no inversion is achieved to up to 200m.

By selecting different wells as a blind spot, to check how the inversion's behavior outside the wells locations, we came to the conclusion that the calibration of the gradient will work better if the sonic log used to obtain the match filter is located in an area with high signal-to-noise ratio. If this requirement is satisfied, the FastWI showed to provide a reasonable inversion at the blind well spot, leading us to assume that the same is reached at any area of the model.

For future work, we will focus to minimize the near-surface limitations, and take advantage of its low computational cost to extend it for 3D surveys.

## ACKNOWLEDGMENTS

The authors thank the sponsors of CREWES for continued support. This work was funded by CREWES industrial sponsors and NSERC (Natural Science and Engineering Research Council of Canada) through the grant CRDPJ 461179-13.

## REFERENCES

- Bishop, T. N., and Spongberg, M. E., 1984, Seismic tomography: A case study: SEG Technical Program Expanded Abstracts, **313**, 712–713.
- Chipman, J. S., 1999, Linear restrictions, rank reduction, and biased estimation in linear regression: Linear Algebra and its Applications, **289**, No. 1, 55 – 74.
- Cutler, R. T., Bishop, T. N., Wyld, H. W., Shuey, R. T., Kroeger, R. A., Jones, R. C., and Rathbun, M. L., 1984, Seismic tomography: Formulation and methodology: SEG Technical Program Expanded Abstracts, **312**, 711–712.
- Fatti, J. L., Smith, G. C., Vail, P. J., Strauss, P. J., and Levitt, P. R., 1994, Detection of gas in sandstone reservoirs using avo analysis: A 3-d seismic case history using the geostack technique: Geophysics, **59**, No. 9, 1362–1376.
- Gavotti, P. E., Lawton, D. C., Margrave, G., and Isaac, J. H., 2012, Post-stack inversion of the hussar low frequency seismic data: CREWES Research Report, **24**, 24.1–24.22.
- Gazdag, J., and Sguazzero, P., 1984, Migration of seismic data by phase shift plus interpolation: Geophysics, **49**, No. 2, 124–131.
- Guarido, M., Lines, L., and Ferguson, R., 2014, Full waveform inversion - a synthetic test using the pspi migration: CREWES Research Report, **26**, 26.1–26.23.

- Guarido, M., Lines, L., and Ferguson, R., 2015, Full waveform inversion: a synthetic test using pspi migration: SEG Technical Program Expanded Abstract, **279**, 1456–1460.
- Guarido, M., Lines, L., and Ferguson, R., 2016, Fwi without tears: a forward modeling free gradient: CREWES Research Report, **28**, 26.1–26.20.
- Guarido, M., Lines, L., and Ferguson, R., 2017a, Forward modeling-free full waveform inversion with well calibration: CREWES Research Report, **29**.
- Guarido, M., Lines, L., and Ferguson, R., 2017b, Fwi without tears: a forward modeling-free gradient: SEG Technical Program Expanded Abstract, 1588–1593.
- Guarido, M., Romahn, S., Lines, L., Ferguson, R., and Innanen, K., 2017c, Comparison of rtm and pspi for obtaining the gradient in the fwi process: CREWES Research Report, **29**.
- Henley, D., 1999, Coherent noise attenuation in the radial trace domain: introduction and demonstration: CREWES Research Report, **11**, 36.1–36.37.
- Lailly, P., 1983, The seismic inverse problem as a sequence of before stack migrations: Conference on inverse scattering, theory and application: Society of Industrial and Applied Mathematics, Expanded Abstracts, 206–220.
- Langan, R. T., Lerche, I., Cutler, R. T., Bishop, T. N., and Spera, N. J., 1984, Seismic tomography: The accurate and efficient tracing of rays through heterogeneous media: SEG Technical Program Expanded Abstracts, **314**, 713–715.
- Lindseth, R. O., 1979, Synthetic sonic logs—a process for stratigraphic interpretation: *Geophysics*, **44**, No. 1, 3–26.
- Lloyd, J. E., and Margrave, G., 2012, Acoustic impedance inversion using stacking velocities: Hussar example: CREWES Research Report, **24**, 60.1–60.10.
- Margrave, G., Bertram, M., Bertram, K., Hall, K., Innanen, K., Lawton, D., Mewhort, L., and Phillips, T., 2012, A low-frequency seismic field experiment: SEG Technical Program Expanded Abstracts 2012, 1–5.
- Margrave, G., Ferguson, R., and Hogan, C., 2010, Full waveform inversion with wave equation migration and well control: CREWES Research Report, **22**, 63.1–63.20.
- Margrave, G., Yedlin, M., and Innanen, K., 2011, Full waveform inversion and the inverse hessian: CREWES Research Report, **23**, 77.1–77.13.
- Pica, A., Diet, J. P., and Tarantola, A., 1990, Nonlinear inversion of seismic reflection data in a laterally invariant medium: *Geophysics*, **55**, No. 2, R59–R80.
- Pratt, R. G., Shin, C., and Hick, G. J., 1998, Gauss-newton and full newton methods in frequency-space seismic waveform inversion: *Geophysical Journal International*, **133**, No. 2, 341–362.
- Romahn, S., and Innanen, K., 2016, Immi: the role of well calibration in the context of high geological complexity: CREWES Research Report, **28**, 66.1–66.17.
- Saeed, A. N., Margrave, G., and Lines, L., 2014, Pre-stack (avo) and post-stack inversion of the hussar low frequency seismic data: CREWES Research Report, **26**, 68.1–68.9.
- Shuey, R. T., 1985, A simplification of the Zoeppritz equations: *Geophysics*, **50**, No. 4, 609–614.
- Tarantola, A., 1984, Inversion of seismic reflection data in the acoustic approximation: *Geophysics*, **49**, No. 8, 1259–1266.
- Virieux, J., and Operto, S., 2009, An overview of full-waveform inversion in exploration geophysics: *Geophysics*, **74**, No. 6, WCC1–WCC26.

Warner, M., and Guasch, L., 2014, Adaptive waveform inversion: Theory: SEG Technical Program Expanded Abstracts, **207**, 1089–1093.

Wenyong, P., Innanen, K., Margrave, G., and Saeed, A. N., 2015, Fwi numerical test using hussar dataset: CREWES Research Report, **27**, 58.1–58.6.

Wenyong, P., Margrave, G., and Innanen, K., 2013, On the role of the deconvolution imaging condition in full waveform inversion: CREWES Research Report, **25**, 72.1–72.19.